

# Close-Packed One-Dimensional Coordination Polymer Cathode with Fast Kinetics for Sodium-Ion Batteries

Yi-An Lo<sup>+</sup><sup>[a]</sup> Trakarn Yimtrakarn<sup>+</sup><sup>[a]</sup> Teng-Hao Chen,<sup>\*[b]</sup> Jui-Chin Lee,<sup>[c]</sup> and Watchareeya Kaveevivitchai<sup>\*[a]</sup>

Sustainable sodium-ion batteries (SIBs) have gained tremendous attention; however, the large-sized  $\text{Na}^+$  poses serious challenges on the development of inorganic-based cathodes. To overcome the issues, metal–organic electrode materials are appealing because they combine attractive characteristics of organic redox centers (e.g., flexibility, highly reversible redox properties, fast kinetics (regardless of size and charge of guest ions), structural/redox tunability, and resource abundance) with structural stability arising from metal-ligand coordination. Herein, a one-dimensional copper–benzoquinoid coordination polymer (CP),  $[\text{CuL}(\text{Py})_2]_n$ , ( $\text{LH}_4 = 1,4\text{-dicyano-2,3,5,6-tetrahydroxybenzene}$ , Py = pyridine) is investigated as cathode for SIBs. As

opposed to most CPs reported for SIBs which possess high porosity and surface area, this close-packed CP can deliver discharge capacity as high as  $277 \text{ mAh g}^{-1}$  at  $2\text{C}$  ( $\sim 523 \text{ mA g}^{-1}$ ), and at extremely high rates of  $50\text{C}$  and  $300\text{C}$  ( $\sim 13$  and  $78 \text{ Ag}^{-1}$ ), reversible capacities of  $131$  and  $74 \text{ mAh g}^{-1}$  still can be delivered, respectively. The transport kinetics of  $\text{Na}^+$  in  $[\text{CuL}(\text{Py})_2]_n$  is found to be even faster than that of  $\text{Li}^+$  despite the close-packed structure. The mechanistic and kinetic studies have been performed. The findings gained in this work undoubtedly unravel a potential design strategy for high-performance metal–organic electrode materials for emerging post-Li-ion batteries.

## Introduction

The rapidly growing demand for large-scale energy storage especially for renewable-energy power grids has propelled the development of better energy storage systems.<sup>[1]</sup> The current lithium-based rechargeable batteries have several major limitations, such as lithium's low natural abundance and high price, the limited energy density of conventional inorganic cathodes, and non-renewable, costly, and toxic transition metals used in electrodes.<sup>[2,3]</sup> This ultimately drives the search for alternative energy storage technologies which are more sustainable. Sodium-ion batteries (SIBs) have shown to be highly attractive in this regard because of inexhaustible resources, widespread availability, and cost effectiveness of sodium and their eco-friendliness. SIBs adopt a “rocking-chair” storage principle similar to the mature lithium-based technologies, which helps materialize the systems more rapidly.<sup>[2]</sup>

Despite these advantages, various challenges still remain in the development of cathode materials for SIBs which has mainly been dominated by inorganic transition-metal-containing materials (such as oxides and polyanions).<sup>[4,5]</sup> This is due to the large size of  $\text{Na}^+$  ( $1.02 \text{ \AA}$  radius vs.  $0.76 \text{ \AA}$  for  $\text{Li}^+$ ), leading to severe lattice distortion, volume change, and phase transition of rigid inorganic crystal structures. The large Na ions are commonly known to have relatively sluggish diffusion kinetics in inorganic lattices with limited capacity and poor cycling stability.<sup>[5]</sup>

To overcome these issues, organic-based compounds which are primarily assembled by weak intermolecular interactions (such as hydrogen bonding and van der Waals forces) are highly promising. The flexible structures of organic electrode materials (as opposed to rigid inorganic lattices) can facilitate the transport of large ions more efficiently.<sup>[6,7]</sup> The reduction/oxidation processes occurring at the redox-active organic functional groups usually involve radical intermediates (which are known for fast kinetics), accompanied by reversible coordination of counter-ions ( $\text{Li}^+$ ,  $\text{Na}^+$ ,  $\text{Zn}^{2+}$ , etc.) with only modest interactions between the soft host lattice and charged guest species. This coordination is known to be much less specific to the nature of the guest metal ions (i.e., regardless of the size or ionic charge), thus allowing organic electrode materials to undergo electron- and ion-storage processes with limited rearrangement of bonds and minimum structural change.<sup>[6–8]</sup> Abundant resources (for C, H, O, N, and S), sustainability, relatively low toxicity, redox tunability (in terms of both specific capacity and redox potential), and structural diversity make organic-based electrodes highly attractive. However, organic materials especially small molecules suffer from dissolution in commonly used organic electrolytes, which prevents these organic compounds from wider adoption.<sup>[9–11]</sup>

[a] Y.-A. Lo,<sup>+</sup> T. Yimtrakarn,<sup>+</sup> W. Kaveevivitchai

Department of Chemical Engineering, Hierarchical Green-Energy Materials (Hi-GEM) Research Center, Academy of Innovative Semiconductor and Sustainable Manufacturing, National Cheng Kung University, Tainan City 70101, Taiwan

E-mail: wkaveechai@mail.ncku.edu.tw

[b] T.-H. Chen

Institute of Clinical Pharmacy and Pharmaceutical Sciences, School of Pharmacy, College of Medicine, National Cheng Kung University, Tainan City 70101, Taiwan

E-mail: thchen@gs.ncku.edu.tw

[c] J.-C. Lee

Core Facility Center, National Cheng Kung University, Tainan City 70101, Taiwan

[+] These authors contributed equally to this work.

Supporting information for this article is available on the WWW under <https://doi.org/10.1002/batt.202400525>

To improve cycling stability, organic moieties may be polymerized via metal-ligand coordination to form crystalline metal-organic coordination polymers (CPs).<sup>[3,12]</sup> By modular design (appropriate selection of the organic or inorganic (metal) modules), the chemical/physical properties and the crystal structure may be fine-tuned for desired applications. The electrochemical performance of CP electrodes can be maximized by utilizing both organic building units and metal nodes which are capable of undergoing redox reactions, thus leading to multi-electron transfer and high theoretical capacity.<sup>[3,12]</sup> In recent years, there have been studies of CPs as electrode materials and electrolytes in various energy storage systems; however, CP cathode materials for SIBs are still rare.<sup>[13–15]</sup> Gallis and co-workers reported the Fe-based MIL-100 as cathode material for both aqueous and non-aqueous SIBs. The results showed good structural stability for over 30 cycles; however, the initial capacity and rate capability were poor, which may be due to low conductivity.<sup>[16,17]</sup> Lee's group reported P(THBQ-Al) which was prepared from benzoquinone-dihydroxydiolate ( $C_6O_6H_2^{2-}$ ) and Al<sup>3+</sup>, possessing superior thermal and structural stability as well as low solubility in non-aqueous electrolytes.<sup>[18]</sup> With the existence of Al metal center, P(THBQ-Al) delivered a much higher capacity (113 mAh g<sup>-1</sup>) compared to the pure organic ligand with stable capacity retention for 100 cycles. It is worth noting that among the limited examples of CPs reported as electrode materials for SIBs, most of them have two- or three-dimensional (2D or 3D) structures with high porosity and surface area,<sup>[19]</sup> which are believed to be crucial for accessible redox centers and fast ionic diffusion, necessary for high-capacity and high-rate applications.

Nevertheless, these porous CPs investigated barely provide satisfactory energy density, rate capability, and cycling stability needed for emerging practical applications.<sup>[20,21]</sup> One plausible reason is due to the fact that CPs with large pores and channels (resulting in low density of redox-active sites) tend to be filled with solvent molecules and counter-anions from the electrolyte, potentially hampering the ionic transport during cell cycling.<sup>[22,23]</sup> Recently, various fascinating examples have shown the significance of supramolecular interactions on the performance of organic-based energy storage systems. These weak non-covalent intermolecular interactions such as  $\pi$ -interactions and H-bonding are believed to assist in stabilizing the structures, leading to unparalleled electrochemical performance.<sup>[9,24,25]</sup> In our previous work, we have demonstrated a proof-of-concept on a 1D close-packed crystalline metal-organic cathode  $[\text{CuL}(\text{Py})_2]_n$ .<sup>[12]</sup> The results reveal that the multiple supramolecular interactions between the close-packed chains are the key factor for Li<sup>+</sup> to desolvate prior to diffusion into the flexible CP structure. These weak interactions also provide additional stabilization to the inserted Li ions in their preferred hopping sites and create optimal pathways for ionic transport. As a result, the material is able to provide exceptional electrochemical performance in Li-ion batteries (LIBs), especially at extremely high rates.<sup>[12]</sup>

To further gain insight into the importance of these supramolecular interactions on the dynamics of large-sized Na<sup>+</sup> ion diffusion, we have investigated 1D  $[\text{CuL}(\text{Py})_2]_n$  CP as cathode

in non-aqueous SIBs. Several *ex situ* and *in situ* characterization techniques have been used to elucidate the redox mechanism of the CP. Interestingly, this close-packed cathode material can deliver a discharge capacity as high as 277 mAh g<sup>-1</sup> at 2C (~523 mA g<sup>-1</sup>), and at extremely high rates of 50C and 300C (~13 and 78 Ag<sup>-1</sup>), reversible capacities of 131 and 74 mAh g<sup>-1</sup> can be delivered, respectively, even after 1000 cycles (for 300C). Interestingly, this rate performance in SIBs appears to be superior to that observed in LIBs from the same cathode material. The desolvation process is found to play a crucial role in determining the electrode kinetics in these two energy storage systems, as revealed by our detailed kinetic studies. These findings undoubtedly unravel a new potential design strategy for high-performance metal-organic electrode materials for SIBs and other newly emerging post-Li-ion batteries.

## Results and Discussion

1D CP with a chemical formula  $[\text{CuL}(\text{Py})_2]_n$  was synthesized according to our previously reported procedure with LH<sub>4</sub> and Cu(NO<sub>3</sub>)<sub>2</sub> as organic linker and metal source, respectively.<sup>[12]</sup> Powder X-ray diffraction (PXRD) was used to confirm the phase purity and crystallinity of the compound, as shown in Figure S1. To briefly describe the crystal structure, Figure 1a shows the repeating unit of the 1D CP chain. The Cu(II) metal center is in octahedral environment and is coordinated by two ligands L via the C=O (or C–O<sup>-</sup>) groups at the *trans*-positions (equatorial), forming 1D linear metal-organic chain.<sup>[12]</sup> The Cu is also capped with two Py molecules in the axial positions. The 1D chains are packed closely with multiple supramolecular interactions, namely,  $\pi\cdots\pi$ , C–H $\cdots\pi$ , C≡N $\cdots\pi$ , and C≡N $\cdots$ H, without any solvent molecules present between the chains (Figure 1b).<sup>[12]</sup>

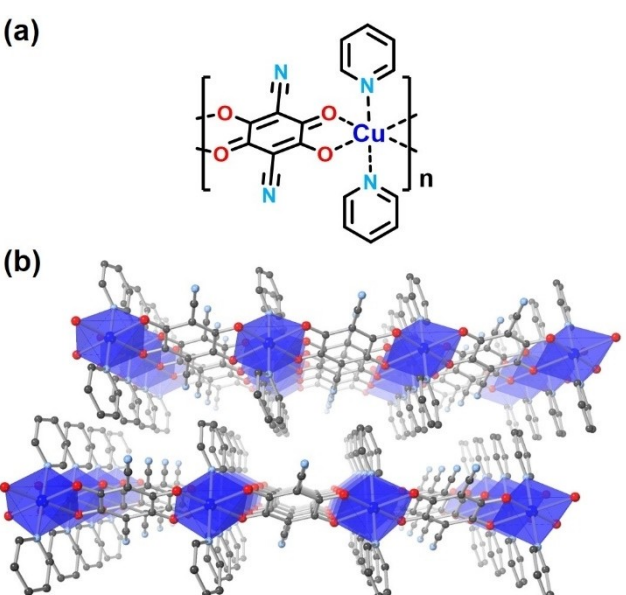


**Figure 1.** (a) Chemical structure of  $[\text{CuL}(\text{Py})_2]_n$ . (b) The single crystal structure of  $[\text{CuL}(\text{Py})_2]_n$  viewed along the x-axis. The hydrogen atoms are omitted for clarity. Colors of atoms: Cu(II), blue octahedron; C, gray; O, red; N, cyan.<sup>[12]</sup>

The  $[\text{CuL}(\text{Py})_2]_n$  CP was electrochemically investigated with Na metal as the counter electrode in the voltage range of 1.1–3.6 V using 1 M  $\text{NaPF}_6$  in ethylene carbonate (EC)/propylene carbonate (PC) (1:1 v/v) as electrolyte. Galvanostatic measurement was carried out as shown in Figure 2. At the rate of 2C ( $\sim 523 \text{ mA g}^{-1}$ ), the CP delivers a specific capacity of  $277 \text{ mAh g}^{-1}$ , which corresponds to  $\sim 3.7$  electron transfer with the capacity contribution from the conducting additive deducted (theoretical capacity =  $65.4 \text{ mAh g}^{-1}$  per electron). Cyclic voltammetry (CV) performed with a scan rate of  $0.2 \text{ mV s}^{-1}$  (Figure 2b) shows several pairs of cathodic/anodic peaks, suggesting that the CP compound undergoes multi-electron redox processes. The organic ligand L redox centers are known to be active at potentials lower than 2.3 V vs.  $\text{Na}/\text{Na}^+$ , while the Cu metal center is believed to be responsible for the redox peaks at a higher potential.<sup>[3,12]</sup> The peak positions in the CV plot appear to be in good agreement with the voltage plateaus observed in the discharge/charge profile in Figure 2a.

The rate capability plot in Figure 2c shows relatively good rate performance of  $[\text{CuL}(\text{Py})_2]_n$ , when the rates are varied from 1C ( $\sim 262 \text{ mA g}^{-1}$ ) to 50C ( $\sim 13 \text{ A g}^{-1}$ ) and then back to 1C, delivering  $\sim 88\%$  capacity retention. The long-term cycling performance of the CP was also tested. Figure 2d shows that there is initial capacity drop before the cells become stabilized. At low rates, the cells can deliver reversible capacities of 196, 163, 152, 146, and  $140 \text{ mAh g}^{-1}$  for 2C, 5C, 10C, 20C, and 50C, respectively. At a very high rate of 50C, the CP provides a capacity retention of 80% after 100 cycles. For extremely high rates of 100C, 150C, 200C, and 300C, the CP can deliver reversible capacities as high as 83, 80, 74, and  $63 \text{ mAh g}^{-1}$ . At 300C ( $\sim 78 \text{ A g}^{-1}$ ), capacity retention of 68% and 54% can be obtained after 1000 and 5000 cycles, respectively. This perform-

ance is superior to several CP electrodes previously reported for SIBs at a similar current density.<sup>[16,18,26,27]</sup> When the ratio of the active material is increased (up to 40 and 50% as shown in Figure S5), the electrochemical performance of the CP is still quite satisfactory (e.g., a reversible capacity of  $\sim 90 \text{ mAh g}^{-1}$  can be obtained even at a very high rate of  $20 \text{ A g}^{-1}$  with 40% active material).

To gain insight into the redox reactions of the CP, several characterization techniques were used. *Ex situ* Fourier-transform infrared (FT-IR) spectroscopy was performed on the CP electrodes. As seen in Figure S7, the carbonyl group of the ligand L can be observed at  $1640 \text{ cm}^{-1}$ . As the cell is discharged down to 2.0 and 1.1 V and the CP undergoes reduction, the relative intensity of the carbonyl group decreases, indicating the interaction between the organic redox center and  $\text{Na}^+$ . As the cell is charged up to 2.4, 2.8, and 3.6 V, the carbonyl peak intensity gradually increases, suggesting that  $\text{Na}$  ions are decoordination as the ligand L is oxidized.<sup>[12]</sup>

To further identify the change in the  $[\text{CuL}(\text{Py})_2]_n$  compound during the redox processes, X-ray photoelectron spectroscopy (XPS) was also carried out on the electrodes. The high-resolution C 1s XPS spectrum (Figure S8) of the CP electrode at 2.5 V (close to open circuit voltage (OCV)) can be deconvoluted into three components at 284.5, 285.4, and 286.9 eV, which are attributed to C–C, C–O, and C=O bonds, respectively.<sup>[3,12,28]</sup> On further discharge down to 1.1 V, the carbonyl group is reduced and transformed into an enolate structure (simultaneously coordinated with positively charged counter-cation  $\text{Na}^+$ ) as witnessed in the relative ratio between C–O and C=O.<sup>[12]</sup> C–O component becomes larger as C=O becomes smaller during discharge, while the reverse process occurs on charge up to 3.6 V. This behavior is consistent with the *ex situ* FT-IR results

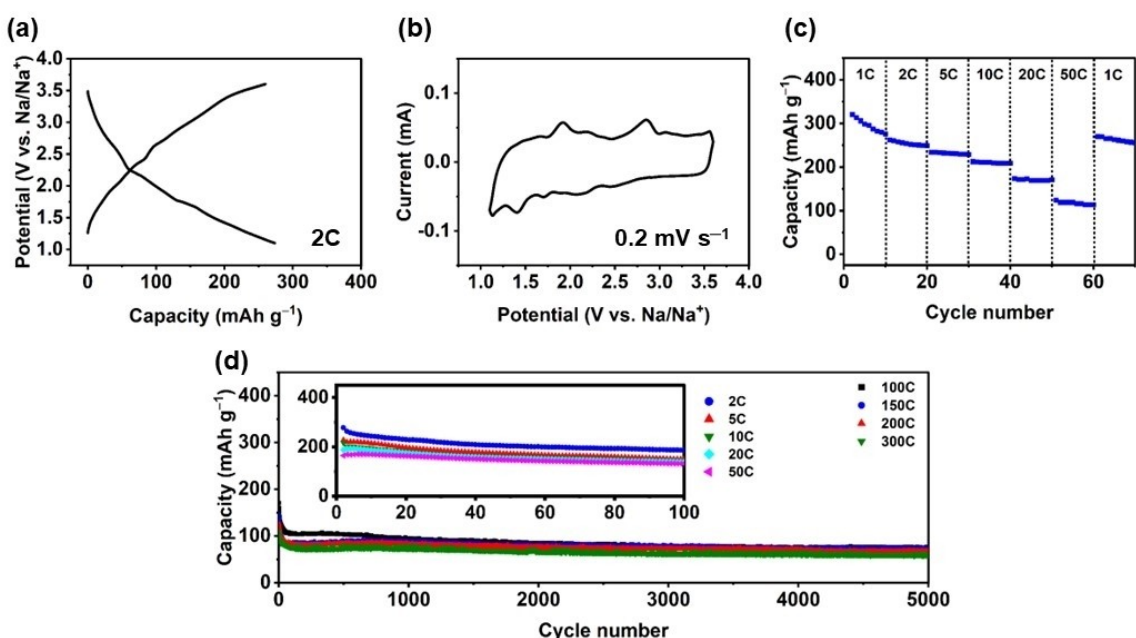


**Figure 2.** Electrochemical behaviors of  $[\text{CuL}(\text{Py})_2]_n$  in Na cells: (a) Galvanostatic discharge/charge curves at a rate of 2C ( $\sim 523 \text{ mA g}^{-1}$ ). (b) CV plot at a scan rate of  $0.2 \text{ mV s}^{-1}$ . (c) Rate capability plot for different rates from 1C ( $\sim 262 \text{ mA g}^{-1}$ ) to 50C ( $\sim 13 \text{ A g}^{-1}$ ). (d) Cycling performance for various rates of 2C to 300C ( $\sim 78 \text{ A g}^{-1}$ ).

and confirms the reversible redox reaction of the organic moieties with the enolate structure converting back to carbonyl on charging.

The deconvolution of the high-resolution Cu 2p spectra in Figure S9 shows that during discharge from 2.5 V down to 1.6 and 1.1 V, the Cu species in the CP gradually undergo reduction as more Cu(0) is observed (Cu 2p<sub>3/2</sub> and Cu 2p<sub>1/2</sub> at 931.9 and 951.6 eV, respectively) and Cu(I) component becomes smaller (Cu 2p<sub>3/2</sub> and Cu 2p<sub>1/2</sub> at 933.2 and 953.1 eV, respectively).<sup>[3,12,29]</sup> During charge up to 2.8 and 3.6 V, Cu(0) obviously becomes less pronounced, while Cu(I) gets stronger. This reveals that the Cu species are reduced and oxidized when the cell is discharged and charged, respectively.

The local environment of the CP metal center and the valence state change were closely monitored by Cu K-edge X-ray absorption spectroscopy (XAS). *In situ* X-ray absorption near edge structure (XANES) experiment was performed during discharge and charge process. During discharge from the pristine state to 1.1 V, the Cu(II) in the CP is gradually reduced as the pre-edge peak is observed at 8982 eV and the edge peak shifts to a lower energy (Figure 3a).<sup>[12,30]</sup> During charge back to 3.6 V (Figure 3b), the curves shift back to a higher photon energy, thus suggesting the Cu species being oxidized. In Figure S10, *ex situ* Cu K-edge extended X-ray absorption fine structure (EXAFS) patterns indicate that the intensity of Cu–O bond becomes weaker at the end of discharge (1.1 V) when compared to that of the pristine, whereas the Cu–Cu bond gets stronger.<sup>[3,12]</sup> At the end of charge (3.6 V), Cu–Cu bond is smaller while Cu–O bond appears larger. This is in agreement with the XPS results mentioned above, confirming the reduction of Cu in the CP structure during discharge and a certain degree of

oxidation during charge. It is evident from both XAS and XPS data that not all the Cu converts back to its original valence of 2+, and this may explain the capacity drop of the CP cathodes during cycling.<sup>[12]</sup>

To further investigate the change in morphology, high-resolution transmission electron microscopy (HR-TEM) imaging was conducted on the CP electrodes at different states of charge. Figure S11 shows that when the CP is discharged, Cu metal nanoparticles are formed with a size of ~5–10 nm, as confirmed by the interplanar spacing of 0.21 nm in the lattice imaging which can be attributed to the (111) plane of Cu metal.<sup>[12]</sup> Figure S11c indicates that at the end of charge, significantly smaller number of Cu nanoparticles can be observed. This agrees well with the electrochemical and other mechanistic studies above which suggest that while the Cu redox centers are shown to be reversible, there is a portion of Cu species remaining as Cu(0). This may be explained by the slow kinetics of Cu–Cu bond dissociation and Cu–O bond formation of the CP during charge.

*In situ* synchrotron PXRD was used to further understand the structural evolution of [CuL(Py)<sub>2</sub>]<sub>n</sub> electrode during cell cycling. As shown in Figures 3d and S12, there is an obvious change in the diffraction patterns. As the cell is discharged from OCV (shown in red), the peak at ~16.6° corresponding to the Miller index plane (hkl)=(101) of the CP slightly shifts to smaller 2θ, which suggests structural expansion due to the reduction of the CP (at both the organic and transition metal redox centers) and the insertion of Na<sup>+</sup> ions.<sup>[12]</sup> When the cell is charged, the peak shifts back to the original position suggesting lattice contraction as the CP is oxidized and Na<sup>+</sup> is extracted. These changes confirm structural integrity and flexibility of [CuL(Py)<sub>2</sub>]<sub>n</sub> during the redox processes which may result from the weak supramolecular interactions.

To gain better understanding of the redox kinetics of [CuL(Py)<sub>2</sub>]<sub>n</sub> electrodes, galvanostatic intermittent titration technique (GITT) was carried out at a low rate of 25 mA g<sup>-1</sup> (~0.1C, Figure 4a), which can be used to obtain quasi-equilibrium potentials at different stages during cell cycling. It is worth noting that at a potential close to the Cu redox couple, the overpotential appears to be larger than that of the organic redox centers especially during charge, which indicates faster redox kinetics of the organic ligand L.<sup>[12]</sup> The Na-ion diffusion coefficients were determined by Fick's second law of diffusion (details in the Supporting Information) to be in the range of 10<sup>-9</sup>–10<sup>-11</sup> cm<sup>2</sup> s<sup>-1</sup> as shown in Figure 4b, which is relatively high for SIBs.<sup>[31,32]</sup> CV curves of [CuL(Py)<sub>2</sub>]<sub>n</sub> at different scan rates in Figure 4c can be used to obtain the relationship between log i (peak current) and log v (scan rate) as shown in Figure 4d. The analysis of charge storage process was performed on the CP with b values calculated from  $i = av^b$ .<sup>[12,33]</sup> The measured current i is fit to a power law with scan rate v, and b can be determined from the slope of the log i vs. log v. This result indicates that the Faradaic charge storage of [CuL(Py)<sub>2</sub>]<sub>n</sub> has a significant capacitive contribution ( $b=0.5$  indicating traditional diffusion dominated charge storage, while  $b=1$  indicating capacitor-like charge storage).<sup>[33,34]</sup>

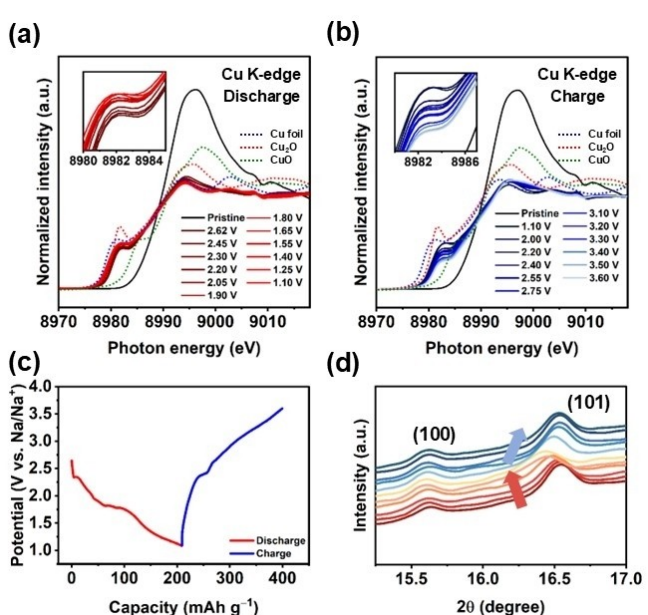


**Figure 3.** *In situ* characterization of [CuL(Py)<sub>2</sub>]<sub>n</sub> cathodes: (a) and (b) *In situ* Cu K-edge XANES patterns during the first discharge and charge, respectively (with Cu foil, Cu<sub>2</sub>O, and CuO as references). (c) Voltage profile of the CP during *in situ* experiment at 50 mA g<sup>-1</sup> (~0.2C). (d) *In situ* synchrotron PXRD data of the CP during the first discharge (dark red) to end of charge (dark blue).

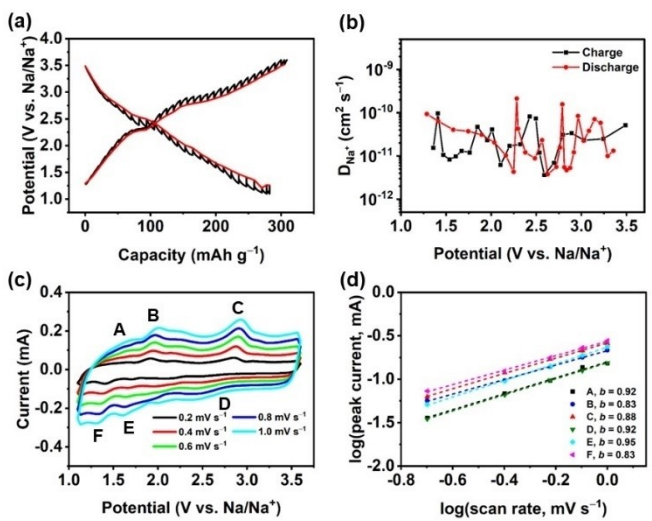


**Figure 4.** (a) GITT discharge/charge curves of  $[\text{CuL}(\text{Py})_2]_n$ . (b) Calculated ionic diffusion coefficients during the discharge/charge processes. (c) Cyclic voltammograms of  $[\text{CuL}(\text{Py})_2]_n$  at various scan rates from 0.2 to 1.0  $\text{mV s}^{-1}$ . (d) Relationship between  $\log i$  (peak current) and  $\log v$  (scan rate) from the CV curves in (c).

Interestingly, the cycling performance of  $[\text{CuL}(\text{Py})_2]_n$  electrodes in Na/[CuL(Py)]<sub>n</sub> cells (with 1 M NaPF<sub>6</sub> in 1:1 v/v EC/PC electrolyte) at different current densities was compared to that of the CP in Li/[CuL(Py)]<sub>n</sub> cells (with 1 M LiPF<sub>6</sub> in 1:1 v/v EC/DMC electrolyte) as shown in Figure S13. It is apparent that within the same voltage window of 2.5 V, the CP in Na cells can provide significantly higher capacity compared to that in Li cells at all rates. This may primarily be related to the electrolyte environment in the two battery systems. Solvation effect is well-known to have a major impact on the electrochemical properties of a system because it affects the solvation shell structure in the bulk electrolyte and the interfacial electrochemical characteristics (the desolvation process at the electrode/electrolyte interphase).<sup>[35–37]</sup> Since the metal salts, NaPF<sub>6</sub> and LiPF<sub>6</sub>, are all PF<sub>6</sub>-based and the solvent systems, EC/PC and EC/DMC (1:1 v/v), are known to have some similar properties (e.g., carbonate solvent molecules (both PC and DMC, each providing only one carbonyl oxygen to solvate Na<sup>+</sup> or Li<sup>+</sup>)),<sup>[35,36]</sup> the electrochemical behavior observed may be explained by the nature of the cations.<sup>[38,39]</sup> The larger Na<sup>+</sup> ion (radius of 1.02 Å vs. 0.76 Å for Li<sup>+</sup>) with a lower charge density (weak Lewis acid) results in weaker interactions with the solvent molecules, thus leading to a smaller Stokes radius and higher diffusion rate.<sup>[38,40]</sup> This also implies smaller desolvation energy and smaller activation energy of Na-ion transfer at the electrode/electrolyte interphase, compared to Li<sup>+</sup> ion. Ultimately, this suggests superior rate performance for the Na<sup>+</sup> system compared to the Li<sup>+</sup> system.<sup>[40]</sup>

To further confirm this observation, temperature-dependent electrochemical impedance spectroscopy (EIS) was performed. Figures 5a and b show the Nyquist plots as a function of temperatures of Na/[CuL(Py)]<sub>n</sub> cell in 1 M NaPF<sub>6</sub> in EC/PC in comparison with Li/[CuL(Py)]<sub>n</sub> cell in 1 M LiPF<sub>6</sub> in EC/DMC

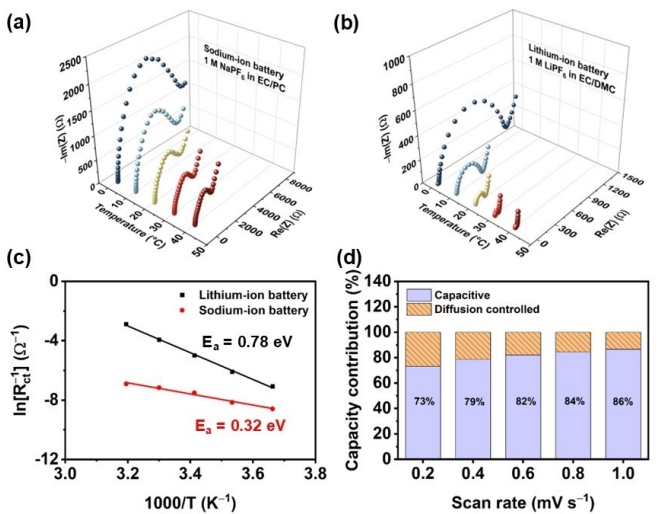


**Figure 5.** Results from kinetic study of  $[\text{CuL}(\text{Py})_2]_n$ : (a) and (b) Temperature-dependent EIS data of Na/[CuL(Py)]<sub>n</sub> cell in 1 M NaPF<sub>6</sub> in 1:1 v/v EC/PC electrolyte and of Li/[CuL(Py)]<sub>n</sub> cell in 1 M LiPF<sub>6</sub> in 1:1 v/v EC/DMC electrolyte, respectively. (c) Arrhenius plots of temperature-dependent EIS resistance comparing the charge transfer activation energy ( $E_{\text{a},\text{ct}}$ ) of the CP in the two systems.<sup>[36]</sup> (d) Capacity contribution plots illustrating diffusion-controlled and capacitive processes obtained from the CV curves of the CP electrode at different scan rates in the NaPF<sub>6</sub> in EC/PC electrolyte according to  $i = k_1v + k_2v^{1/2}$ .<sup>[41–43]</sup>

electrolyte. Figure 5c reveals the Arrhenius plots which indicate the charge transfer activation energy ( $E_{\text{a},\text{ct}}$ ) in the two electrolyte systems, 0.78 eV for the Li<sup>+</sup> which is more than twice the value from the Na<sup>+</sup> system (0.32 eV). As a result, the Na-ion transport across the interphase would be faster, leading to better rate capability.<sup>[35,36]</sup> Moreover, the flexible close-packed 1D metal-organic CP chains of  $[\text{CuL}(\text{Py})_2]_n$  which are also held together by supramolecular interactions are known to only allow desolvated guest ions (Li<sup>+</sup> or Na<sup>+</sup>) to intercalate.<sup>[12]</sup> As a result, Na<sup>+</sup> ions with smaller desolvation energy and lower activation energy  $E_{\text{a},\text{ct}}$  would have better transport kinetics, leading to much higher rate performance and higher specific capacity at any current density compared to the Li system with the same CP cathode material.<sup>[36,40]</sup>

Moreover, the co-insertion of the PF<sub>6</sub><sup>-</sup> from the electrolyte into the CP has also been ruled out (according to single-crystal XRD and *ex situ* FT-IR from our previous work).<sup>[12]</sup> Without co-intercalation of the anions and solvent molecules, facile transport of the guest ions may be expected. Without the large anions and solvents co-inserted, the overall structural integrity can be maintained during long-term cycling, as evidenced in the *in situ* synchrotron PXRD data. The weak intermolecular interactions between the CP chains have also been proved to help stabilize the inserted cations in the preferred hopping sites (with surrounding oxygen and nitrogen atoms from ligand L and coordinated Py molecule), thereby allowing optimal diffusion paths for guest cations to transport efficiently in three dimensions.<sup>[12]</sup>

To quantitatively differentiate the contribution from the capacitive and diffusion-controlled processes to the overall capacity, the CV results at various scan rates (Figure 4c) were

used (Figure 5d, details in the Supporting Information).<sup>[41–43]</sup> It has been found that the ratio of stored charge contributed by capacitive process increases with the scan rate. For all of the scan rates tested, capacitive contribution appears to be largely dominating, which confirms the non-diffusion-controlled charge storage process and excellent rate performance of  $[\text{CuL}(\text{Py})_2]_n$  cathode. The pseudocapacitive behavior of charge storage observed in this cathode material may arise from the dense redox-active sites of the close-packed CP, yet with accessible and well-defined ion transport pathways, as well as the highly reversible charge- and ion-storage of the organic redox centers which is known for fast kinetics and stabilized intermediates (electron delocalization by resonance effect).<sup>[5,44,45]</sup> Similar pseudocapacitive behavior can also be found in many organic-based electrode materials.<sup>[41,44,46]</sup>

## Conclusions

1D CP  $[\text{CuL}(\text{Py})_2]_n$  has been shown to have interesting electrochemical properties as cathode in SIBs. Despite the close-packed structure, the CP is capable of undergoing reversible Na-ion/electron storage (up to 3.7 electron transfer) with both the organic ligand L and the Cu metal center being redox-active. Several *in situ* and *ex situ* characterization techniques have been used to elucidate the redox mechanism, with reversible carbonyl/enolate transformation and the reduction/oxidation of the Cu accompanied by the insertion/extraction of Na ions to maintain charge neutrality during discharge and charge, respectively. Even with the large-sized  $\text{Na}^+$  which has been shown to have sluggish transport kinetics in conventional inorganic cathodes, the CP can be cycled at extremely high rates up to 300C ( $\sim 78 \text{ A g}^{-1}$ ) with remarkable reversible capacities up to 5000 cycles. To the best of our knowledge,  $[\text{CuL}(\text{Py})_2]_n$  is the first close-packed 1D CP to be used as cathode for SIBs with superior rate capability. Surprisingly, the  $\text{Na}^+$  transport kinetics in  $[\text{CuL}(\text{Py})_2]_n$  cathode has been found superior to that of  $\text{Li}^+$  in the same material, as evidenced by the much lower  $E_{\text{a},\text{ct}}$  of  $\text{Na}^+$ . This is presumably due to the weaker Lewis acidity of  $\text{Na}^+$ , which results in weaker interactions with the solvent molecules (smaller desolvation energy) and thereby a smaller Stokes radius and higher ionic diffusion rate. The close-packed CP chains of  $[\text{CuL}(\text{Py})_2]_n$  cathode with multiple supramolecular interactions also facilitate desolvation of the cations, leading to more rapid  $\text{Na}^+$  transport across electrode/electrolyte interphase and therefore better rate capability and higher capacity compared to  $\text{Li}^+$ . Although the CP still has an issue with Cu deep reduction affecting cycling stability especially at low rates, the performance at high rates is found to be exceptional even with a close-packed structure of the cathode, which is in contrast with many metal-organic electrode materials utilizing high porosity for faster ionic diffusion. These findings are invaluable for the design of next-generation high-performance sustainable electrode materials.

## Acknowledgements

This work was supported by the National Science and Technology Council (NSTC) of Taiwan under grants NSTC 112-2113-M-006-004 (to T.-H. C.), NSTC 111-2221-E-006-011-MY3, and 112-2221-E-006-021-MY3 (to W. K.). This work was also financially supported by the Hierarchical Green-Energy Materials (Hi-GEM) Research Center, from the Featured Areas Research Center Program within the framework of the Higher Education Sprout Project by the Ministry of Education (MOE) in Taiwan (to W. K.). This research was supported in part by High Education Sprout Project, MOE of the Headquarters of University Advancement at National Cheng Kung University (NCKU) (to T.-H. C. and W. K.). The authors gratefully acknowledge the use of ESCA000200, ESCA003700, and EM000800 of NSTC 112-2740-M-006-001 belonging to the Core Facility Center of NCKU.

## Conflict of Interests

The authors declare no conflict of interest.

## Data Availability Statement

The data that support the findings of this study are available from the corresponding author upon reasonable request.

**Keywords:** Sodium-ion batteries · Supramolecular interactions · Coordination polymers · Quinone · Cathode material

- [1] Y. Liang, Y. Yao, *Joule* **2018**, *2*, 1690–1706.
- [2] H. Wang, P. Hu, J. Yang, G. Gong, L. Guo, X. Chen, *Adv. Mater.* **2015**, *27*, 2348–2354.
- [3] C.-H. Chang, A.-C. Li, I. Popovs, W. Kaveevivitchai, J.-L. Chen, K.-C. Chou, T.-S. Kuo, T.-H. Chen, *J. Mater. Chem. A* **2019**, *7*, 23770–23774.
- [4] M. Lee, J. Hong, J. Lopez, Y. Sun, D. Feng, K. Lim, W. C. Chueh, M. F. Toney, Y. Cui, Z. Bao, *Nat. Energy* **2017**, *2*, 861–868.
- [5] Y. Hu, Q. Yu, W. Tang, M. Cheng, X. Wang, S. Liu, J. Gao, M. Wang, M. Xiong, J. Hu, C. Liu, T. Zou, C. Fan, *Energy Storage Mater.* **2021**, *41*, 738–747.
- [6] C. Ma, L.-Y. Wang, M.-H. Shu, C.-C. Hou, K.-X. Wang, J.-S. Chen, *J. Mater. Chem. A* **2021**, *9*, 11530–11536.
- [7] S. Wu, W. Wang, M. Li, L. Cao, F. Lyu, M. Yang, Z. Wang, Y. Shi, B. Nan, S. Yu, Z. Sun, Y. Liu, Z. Lu, *Nat. Commun.* **2016**, *7*, 13318.
- [8] R. R. Kapaev, I. S. Zhidkov, E. Z. Kurmaev, K. J. Stevenson, P. A. Troshin, *J. Mater. Chem. A* **2019**, *7*, 22596–22603.
- [9] M.-S. Wu, N. T. H. Luu, T.-H. Chen, H. Lyu, T.-W. Huang, S. Dai, X.-G. Sun, A. S. Ivanov, J.-C. Lee, I. Popovs, W. Kaveevivitchai, *Adv. Energy Mater.* **2021**, *11*, 2100330.
- [10] N. T. H. Luu, A. S. Ivanov, T.-H. Chen, I. Popovs, J.-C. Lee, W. Kaveevivitchai, *J. Mater. Chem. A* **2022**, *10*, 12371–12377.
- [11] S. Lee, G. Kwon, K. Ku, K. Yoon, S.-K. Jung, H.-D. Lim, K. Kang, *Adv. Mater.* **2018**, *30*, 1704682.
- [12] A.-C. Li, C.-H. Chang, A. S. Ivanov, Y.-A. Lo, I. Popovs, J.-L. Chen, Y.-C. Chuang, Y.-C. Chang, B.-H. Chen, J.-C. Lee, T.-H. Chen, W. Kaveevivitchai, *J. Mater. Chem. A* **2022**, *10*, 19671–19679.
- [13] Z. Wu, J. Xie, Z. J. Xu, S. Zhang, Q. Zhang, *J. Mater. Chem. A* **2019**, *7*, 4259–4290.
- [14] A. K. Thakur, M. Majumder, S. P. Patole, K. Zaghib, M. V. Reddy, *Mater. Adv.* **2021**, *2*, 2457–2482.
- [15] R. Mehek, N. Iqbal, T. Noor, M. Z. B. Amjad, G. Ali, K. Vignarooban, M. A. Khan, *RSC Adv.* **2021**, *11*, 29247–29266.

- [16] D. F. Sava Gallis, H. D. Pratt III, T. M. Anderson, K. W. Chapman, *J. Mater. Chem. A* **2016**, *4*, 13764–13770.
- [17] J. S. Chavez, Katharine L. Harrison, D. F. Sava Gallis, *RSC Adv.* **2017**, *7*, 24312–24320.
- [18] H. J. Kim, Y. Kim, J. Shim, K. H. Jung, M. S. Jung, H. Kim, J.-C. Lee, K. T. Lee, *ACS Appl. Mater. Interfaces* **2018**, *10*, 3479–3486.
- [19] M. Wang, R. Dong, X. Feng, *Chem. Soc. Rev.* **2021**, *50*, 2764–2793.
- [20] Z. Zhang, H. Yoshikawa, K. Awaga, *J. Am. Chem. Soc.* **2014**, *136*, 16112–16115.
- [21] W. Kaveevivitchai, A. J. Jacobson, *J. Power Sources* **2015**, *278*, 265–273.
- [22] L. Liu, X. Chen, W. Lu, A. Han, Y. Qiao, *Phys. Rev. Lett.* **2009**, *102*, 184501.
- [23] M. E. Ziebel, C. A. Gaggioli, A. B. Turkiewicz, W. Ryu, L. Gagliardi, J. R. Long, *J. Am. Chem. Soc.* **2020**, *142*, 2653–2664.
- [24] K. Nakashima, T. Shimizu, Y. Kamakura, A. Hinokimoto, Y. Kitagawa, H. Yoshikawa, D. Tanaka, *Chem. Sci.* **2020**, *11*, 37–43.
- [25] L. Sieuw, A. Jouhara, É. Quarez, C. Auger, J.-F. Gohy, P. Poizot, A. Vlad, *Chem. Sci.* **2019**, *10*, 418–426.
- [26] T. Shimizu, T. Mameuda, H. Toshima, R. Akiyoshi, Y. Kamakura, K. Wakamatsu, D. Tanaka, H. Yoshikawa, *ACS Appl. Energy Mater.* **2022**, *5*, 5191–5198.
- [27] K. Wakamatsu, S. Furuno, Y. Yamaguchi, R. Matsushima, T. Shimizu, N. Tanifugi, H. Yoshikawa, *ACS Appl. Energy Mater.* **2023**, *6*, 9124–9135.
- [28] J. Wang, Q. Deng, M. Li, K. Jiang, J. Zhang, Z. Hu, J. Chu, *Sci. Rep.* **2017**, *7*, 8903.
- [29] Z. Jin, C. Liu, K. Qi, X. Cui, *Sci. Rep.* **2017**, *7*, 39695.
- [30] H. H. Lee, J. B. Lee, Y. Park, K. H. Park, M. S. Okyay, D.-S. Shin, S. Kim, J. Park, N. Park, B.-K. An, Y. S. Jung, H.-W. Lee, K. T. Lee, S. Y. Hong, *ACS Appl. Mater. Interfaces* **2018**, *10*, 22110–22118.
- [31] W. Ren, M. Qin, Z. Zhu, M. Yan, Q. Li, L. Zhang, D. Liu, L. Mai, *Nano Lett.* **2017**, *17*, 4713–4718.
- [32] Y.-S. Lee, K.-S. Ryu, *Sci. Rep.* **2017**, *7*, 16617.
- [33] Q. Jiang, P. Xiong, J. Liu, Z. Xie, Q. Wang, X.-Q. Yang, E. Hu, Y. Cao, J. Sun, Y. Xu, L. Chen, *Angew. Chem. Int. Ed.* **2020**, *59*, 5273–5277.
- [34] J. B. Cook, H.-S. Kim, T. C. Lin, C.-H. Lai, B. Dunn, S. H. Tolbert, *Adv. Energy Mater.* **2017**, *7*, 1601283.
- [35] H.-C. Kuan, N. T. H. Luu, A. S. Ivanov, T.-H. Chen, I. Popovs, J.-C. Lee, W. Kaveevivitchai, *J. Mater. Chem. A* **2022**, *10*, 16249–16257.
- [36] T. Sun, X.-L. Feng, Q.-Q. Sun, Y. Yu, G.-B. Yuan, Q. Xiong, D.-P. Liu, X.-B. Zhang, Y. Zhang, *Angew. Chem. Int. Ed.* **2021**, *60*, 26806–26812.
- [37] K. Xu, Y. Lam, S. S. Zhang, T. R. Jow, T. B. Curtis, *J. Phys. Chem. C* **2007**, *111*, 7411–7421.
- [38] K.-i. Saitoh, Y. Takai, T. Sato, M. Takuma, Y. Takahashi, *Batteries* **2022**, *8*, 27.
- [39] X. Bogle, R. Vazquez, S. Greenbaum, A. v. W. Cresce, K. Xu, *J. Phys. Chem. Lett.* **2013**, *4*, 1664–1668.
- [40] E. J. Kim, P. R. Kumar, Z. T. Gossage, K. Kubota, T. Hosaka, R. Tatara, S. Komaba, *Chem. Sci.* **2022**, *13*, 6121–6158.
- [41] W. Wang, V. S. Kale, Z. Cao, S. Kandambeth, W. Zhang, J. Ming, P. T. Parvatkar, E. Abou-Hamad, O. Shekhar, L. Cavallo, M. Eddaoudi, H. N. Alshareef, *ACS Energy Lett.* **2020**, *5*, 2256–2264.
- [42] Z. Lin, H.-Y. Shi, L. Lin, X. Yang, W. Wu, X. Sun, *Nat. Commun.* **2021**, *12*, 4424.
- [43] J. Wang, J. Polleux, J. Lim, B. Dunn, *J. Phys. Chem. C* **2007**, *111*, 14925–14931.
- [44] M. Yu, N. Chandrasekhar, R. K. M. Raghupathy, K. H. Ly, H. Zhang, E. Dmitrieva, C. Liang, X. Lu, T. D. Kühne, H. Mirhosseini, I. M. Weidinger, X. Feng, *J. Am. Chem. Soc.* **2020**, *142*, 19570–19578.
- [45] M. Yu, R. Dong, X. Feng, *J. Am. Chem. Soc.* **2020**, *142*, 12903–12915.
- [46] Z. Ye, S. Xie, Z. Cao, L. Wang, D. Xu, H. Zhang, J. Matz, P. Dong, H. Fang, J. Shen, M. Ye, *Energy Storage Mater.* **2021**, *37*, 378–386.
- [47] C. Fang, Y. Huang, L. Yuan, Y. Liu, W. Chen, Y. Huang, K. Chen, J. Han, Q. Liu, Y. Huang, *Angew. Chem. Int. Ed.* **2017**, *56*, 6793–6797.
- [48] M. L. Aubrey, J. R. Long, *J. Am. Chem. Soc.* **2015**, *137*, 13594–13602.
- [49] Y. Chen, Q. Zhu, K. Fan, Y. Gu, M. Sun, Z. Li, C. Zhang, Y. Wu, Q. Wang, S. Xu, J. Ma, C. Wang, W. Hu, *Angew. Chem. Int. Ed.* **2021**, *60*, 18769–18776.
- [50] Y. Wu, Y. Chen, M. Tang, S. Zhu, C. Jiang, S. Zhuo, C. Wang, *Chem. Commun.* **2019**, *55*, 10856–10859.
- [51] G. Ding, L. Zhu, Q. Han, L. Xie, X. Yang, X. Li, L. Chen, G. Wang, F. Sun, X. Cao, *ACS Appl. Energy Mater.* **2021**, *4*, 8538–8549.
- [52] K. Fan, C. Fu, Y. Chen, C. Zhang, G. Zhang, L. Guan, M. Mao, J. Ma, W. Hu, C. Wang, *Adv. Sci.* **2023**, *10*, 2205760.
- [53] L. Cheng, J. Yu, L. Chen, J. Chu, J. Wang, H.-G. Wang, D. Feng, F. Cui, G. Zhu, *Small* **2023**, *19*, 2301578.
- [54] K. Fan, J. Li, Y. Xu, C. Fu, Y. Chen, C. Zhang, G. Zhang, J. Ma, T. Zhai, C. Wang, *J. Am. Chem. Soc.* **2023**, *145*, 12682–12690.
- [55] L. Wang, N. Liu, X. Zhao, X. Wang, T. Zhang, Z. Luo, F. Li, *Chem. Sci.* **2024**, *15*, 2133–2140.
- [56] M. Qi, L. Cheng, H.-G. Wang, F. Cui, Q. Yang, L. Chen, *Adv. Mater.* **2024**, *36*, 2401878.

Manuscript received: July 31, 2024

Revised manuscript received: October 8, 2024

Accepted manuscript online: October 29, 2024

Version of record online: November 19, 2024